Research Article

Effect of sintering temperature in argon atmosphere on microstructure and properties of 3D printed alumina ceramic cores

He LI[a,b], Yongsheng LIU[a,b,*], Yansong LIU[a,b], Qingfeng ZENG[a,*],
Kehui HU[c,d], Zhigang LU[c,d], Jingjing LIANG[e]

[a]*Science and Technology on Thermostructural Composite Materials Laboratory,*
Northwestern Polytechnical University, Xi'an, Shaanxi 710072, China
[b]*NPU-SAS Joint Research Center of Advanced Ceramics, Northwestern*
Polytechnical University, Xi'an, Shaanxi 710072, China
[c]*Department of Mechanical Engineering, Tsinghua University, Beijing 100084, China*
[d]*State Key Laboratory of Tribology, Tsinghua University, Beijing 100084, China*
[e]*Institute of Metal Research, Chinese Academy of Sciences, Shenyang 110016, China*

Abstract: Alumina ceramics with different sintering temperatures in argon atmosphere were obtained using stereolithography-based 3D printing. The effects of sintering temperature on microstructure and physical and mechanical properties were investigated. The results show that the average particle size, shrinkage, bulk density, crystallite size, flexural strength, Vickers hardness, and nanoindentation hardness increased with the increase in sintering temperature, whereas the open porosity decreased with increasing sintering temperature. No change was observed in phase composition, chemical bond, atomic ratio, and surface roughness. For the sintered samples, the shrinkage in *Z* direction is much greater than that in *X* or *Y* direction. The optimum sintering temperature in argon atmosphere is 1350 ℃ with a shrinkage of 3.0%, 3.2%, and 5.5% in *X*, *Y*, and *Z* directions, respectively, flexural strength of 26.7 MPa, Vickers hardness of 198.5 HV, nanoindentation hardness of 33.1 GPa, bulk density of 2.5 g/cm^3, and open porosity of 33.8%. The optimum sintering temperature was 70 ℃ higher than that sintering in air atmosphere when achieved the similar properties.

Keywords: sintering temperature; argon atmosphere; alumina ceramics; microstructure; stereolithography

1 Introduction

Turbine blade designers and manufacturers aim to continuously improve the cooling structure and efficiency of blades, and one of the key technologies is the manufacturing of ceramic core [1,2]. The alumina ceramic cores possess good chemical stability and creep resistance, ensuring the dimensional accuracy and pass rate of directional columnar and single crystal hollow blades with a complex inner cavity structure and reducing the manufacturing cost of blades [3]. The alumina-based ceramic cores could withstand higher operation temperature than silica-based ceramic cores due to its excellent anti-sustained high temperature

---

* Corresponding authors.
E-mail: Y. Liu, yongshengliu@nwpu.edu.cn;
        Q. Zeng, qfzeng@nwpu.edu.cn

capability. However, there are many problems in the forming method of alumina ceramic cores in practical production, restricting the application of alumina ceramic cores [4]. Traditionally, alumina ceramic cores are prepared using investment casting method, requiring a long cycle production period with low precision and complex process [5].

In recent years, because of the rise of 3D printing technology in the field of ceramics, it provides a rapid and accurate preparation method for complex ceramic parts [6–9]. However, ceramic components prepared using stereolithography 3D printing technology usually have a higher shrinkage and easy to crack [10]. Chen *et al.* [11] prepared cordierite ceramic parts with a shrinkage of 33.7%–60.8% using stereolithography-based 3D printing method and found that distinct features of cracks are demonstrated on different surfaces of as-printed samples. Liu *et al.* [12] fabricated zirconia-based ceramics using stereolithography with a shrinkage of 20.0%–22.4% for the sintered samples. He *et al.* [13] fabricated complex-shaped zirconia ceramic parts via stereolithography with a shrinkage of 35.3%. Although many studies have been conducted to improve the 3D printing technology, the shrinkage of ceramic is still very large.

Except the deformation caused by excessive shrinkage, alumina ceramic cores still should satisfy the requirements of open porosity and flexural strength. Because the ceramic cores should be removed, its open porosity should be greater than 30%. During the preparation of hollow turbine blades, the ceramic cores should be able to withstand a certain amount of impact; therefore, its flexural strength should be greater than 20 MPa [14–19].

As the rate of argon diffusion was slightly lower than oxygen, the sintering process was slightly different compared to the sintering in air atmosphere [20–22]. Ben Ayed *et al.* [23] reported that the use of argon as sintering atmosphere helps to maintain the density of sintered bodies at its highest value at much higher temperatures. Mandal *et al.* [24] reported that the weight loss of SiC–γ-AlON composite was higher when sintered in argon than nitrogen. Mulla and Krstic [25] reported that argon atmosphere exceeds the rate of densification for β-SiC with Al_2O_3 additions. As sintering could determine the microstructure of ceramics, this study aims to optimize the sintering process to control the physical and mechanical properties of ceramics. When sintered in different atmospheres, the gases present in the pores of ceramics are different, and their rate of diffusion

is also different, causing different growths of particles [26–28], which would change the properties of sintered ceramics. Therefore, argon atmosphere was used in this study to evaluate the effect of sintering temperature on the microstructure and mechanical properties of 3D-printed alumina ceramics. Several characterization and test methods were used to analyze and evaluate the sintered alumina ceramics.

2 Experimental

2.1 Fabrication of alumina green bodies

A 3D printer (AutoceraM, Beijing Ten Dimensions Technology Co., Ltd., China) equipped with a LED light source of 405 nm wavelength was used to print alumina green bodies (50 mm × 4 mm × 3 mm). During the printing, the exposure energy was 10 mW/cm², the single layer exposure time was 10 s, and the layer thickness was 0.1 mm. To prepare ceramic slurries, alumina powders (AW-SF, Henan Hecheng Inorganic New Material Co., Ltd., China) were dried at 200 ℃ for 5 h in a blast air oven. Ceramic slurry was prepared as follows: 495 g of Al_2O_3 powder was added to 100 g photosensitive resin (Al100-1, Beijing Ten Dimensions Technology Co., Ltd., China) slowly, and the reaction mixture was stirred vigorously. It was ball-milled for 2 h using a planet-type grinding mill at a rate of 400 rpm after the slurries were stirred evenly. Then, the slurries were vacuum defoamed for 10 min to obtain the alumina ceramic slurry.

2.2 Debinding and sintering processes

The green bodies underwent debinding and presintering in a muffle furnace (Hefei Ke Jing Materials Technology Co., Ltd., China). First, the samples were heated to 200 ℃ with a heating rate of 2 ℃/min. Second, the samples were heated to 550 ℃ with a heating rate of 1 ℃/min and maintained for 2 h. Third, the samples were heated to 1000 ℃ with a heating rate of 5 ℃/min and maintained for 2 h. Finally, the samples were cooled to 600 ℃ with a heating rate of 5 ℃/min and subsequently subjected to furnace cooling. These processes were carried out in air atmosphere. The debinding and presintering profile is shown in Fig. 1(a).

Then, the samples were transferred to a tube furnace (Hefei Ke Jing Materials Technology Co., Ltd., China). First, the samples were heated to 200 ℃ with a heating
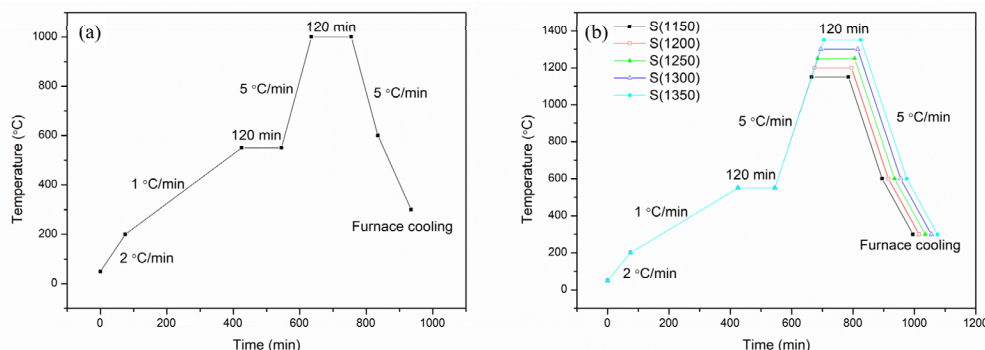
Fig. 1 (a) Debinding, presintering, and (b) sintering processes of green bodies.

rate of 2 ℃/min. Second, the samples were heated to 550 ℃ with a heating rate of 1 ℃/min and maintained for 2 h. Third, the samples were heated to the target temperature T (T = 1150, 1200, 1250, 1300, 1350 ℃) with a heating rate of 5 ℃/min and maintained for 2 h. Finally, the samples were cooled to 600 ℃ with a heating rate of 5 ℃/min and subsequently subjected to furnace cooling. These processes were carried out in argon atmosphere. The sintering profile is shown in Fig. 1(b). The samples were denoted as S(T), and T = 1150, 1200, 1250, 1300, 1350 ℃.

2. 3 Characterization

X-ray diffraction (XRD) patterns were recorded using a Bruker D8 FOCUS (Bruker Corporation, Germany) X-ray diffractometer equipped with Cu Kα radiation. The diffraction angle 2θ was scanned from 10° to 90°. The voltage was 40 kV, and the generator current was 30 mA. The scan rate was 0.02 (°)/s per step. The crystallite size of alumina was calculated using the Scherrer's equation from the peak at 2θ = 35.3° as follows [29].

$$d = \frac{K\lambda}{B\cos\theta} \tag{1}$$

where d is the average crystallite size of alumina (nm), K is the Scherrer constant (0.89 in this case), λ is the wavelength of X-ray (0.154056 nm), and B is the peak width at half height of alumina.

The Raman spectra of samples were measured using a Confocal Raman Microscope system (Alpha300R, WITec) with a laser source of 532 nm, power of 50 mW, and slit width of 50 μm. X-ray photoelectron spectroscopy (XPS) was performed using an Axis Supra (Shimadzu) photoelectron spectrometer. Scanning electron microscopy (SEM) images were obtained from Helios G4 CX (FEI Corporation). Transmission electron microscopy (TEM)

images were obtained from Tecnai G2 F20 (FEI Corporation). Energy spectrum analysis (EDS) was also conducted to obtain elemental distribution.

The bulk density of sintered samples was measured using the Archimedes method [30]. The accuracy of balance was 0.0001 g (Mettler Toledo, Switzerland).

The flexural strength of sintered samples was tested using an electronic universal testing machine (CMT4304, SUNS, China) using the three-point flexure method [31]. The loading speed was 0.5 mm/min, and the span was 30 mm.

The surface roughness of sample was measured by atomic force microscopy (Dimension Icon, Bruker, USA), and the spring constant was 0.40 N/m [32].

The nanoindentation test was performed using a nano-test apparatus (TI980, Hysitron, USA). Static indentation test was carried out at room temperature. First, the head approaches the surface of sample at a speed of 2 mN/s, and after contacting the sample, it is loaded to the maximum load of 10 mN using 5 s for loading and unloaded using 5 s after reaching the maximum load sustained for 2 s. The load–displacement curve was recorded using the connected computer during the entire test, and five points were tested for each sample [33].

The Vickers hardness test was performed using a Micro/Macro Automatic Hardness Testing (LM248AT, LECO, USA). The load was 1000 g, the dwell was 15 s, and five points were tested for each sample.

3 Results and discussion

3. 1 Microstructure and composition

The microstructure observed by SEM is shown in Fig. 2. The results show that all the samples sintered at different temperatures exhibited delamination. Cracks were
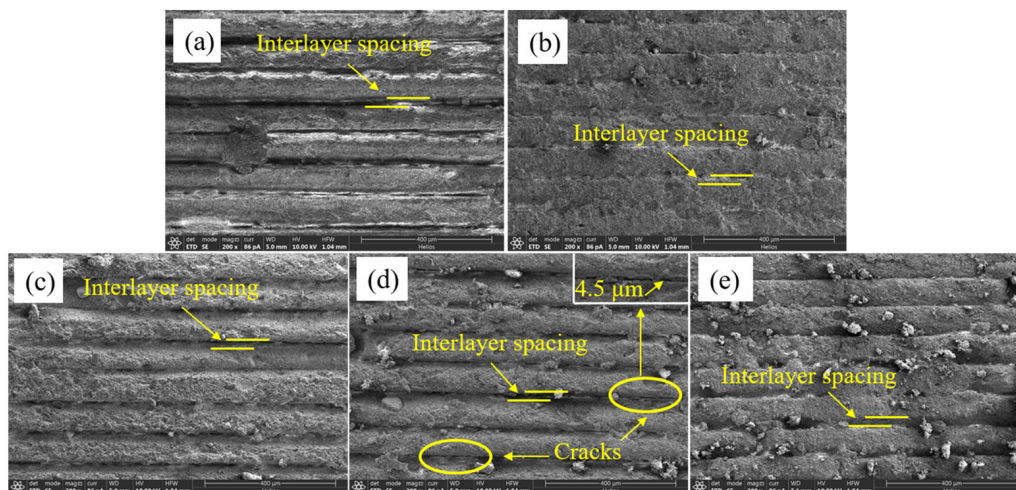
Fig. 2 Sintered samples observed by SEM at (a) 1150, (b) 1200, (c) 1250, (d) 1300, and (e) 1350 ℃.

observed in the samples sintered at 1300 ℃, and the size of cracks was 4.5 μm. The interlayer spacing of different samples is shown in Fig. 3, indicating that the interlayer spacing first decreases and then increases with increasing sintering temperature in argon. As the samples were fabricated using 3D printing forming method, the binding force of alumina particles in *X–Y* plane is different from that in *Z* direction. After debinding and sintering, the weak binding force of alumina particles in *Z* direction shows the spacing among layers. The sintering driving force is very low when sintered at 1150 ℃, leading to weak binding force of alumina particles. This resulted in a relatively greater interlayer spacing for sintered alumina ceramics. As the sintering temperature was increased to 1200 ℃, the increased sintering driving force promoted the bonding of layers together, thus decreasing the interlayer spacing. However, as the sintering temperature continued to increase, the densification process would promote the shrinkage of sintered alumina ceramic, thus increasing the interlayer spacing. In the range of 1200–1350 ℃, the interlayer spacing was increasing as the sintering temperature increased. Higher sintering temperature promotes the shrinkage process of the sintered ceramics. The distance of the particles between adjacent layers increases as the increasing sintering temperature, which exhibited the increasing interlayer spacing phenomenon. A layer-by-layer phenomenon also existed in the dense alumina ceramics fabricated using stereolithography method. Schwentenwein and Homa [34] sintered alumina ceramic at 1600 ℃ prepared using stereolithography and found that on the outside of fabricated objects, grooves from the layer boundaries exist at a microscopic level.
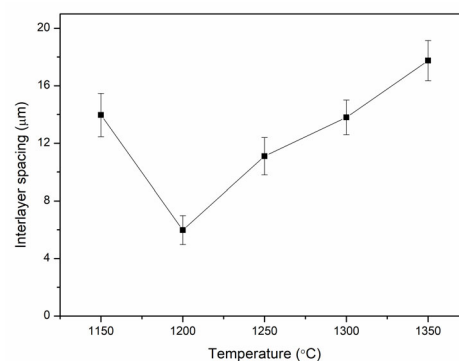

Fig. 3 Variation tendency of interlayer spacing sintered at different temperatures.

The microstructure of alumina ceramics sintered at different temperatures is shown in Fig. 4. Connected borders, unconnected borders, and pores were observed in each sample, indicating that a large number of voids exist in the alumina ceramics. As the green bodies were composed of photosensitive resin and alumina powders, the photosensitive resin was volatilized during debinding [35], subsequently forming voids due to the removal of photosensitive resin. Then, a large number of alumina powders connected together due to sintering. The average particle size of alumina ceramics sintered at different temperatures is shown in Fig. 5, indicating that the average particle size increased with increasing the sintering temperature, i.e., a higher sintering temperature would promote the growth of particles. This is a common phenomenon observed in other ceramics, Hahn *et al.* [36] monitored the grain growth of sintered TiO_2 using XRD and SEM and found that the grain growth begins at 600 ℃ and rapidly accelerates at 1000 ℃. Pookmanee *et al.* [37] observed the microstructure of sodium titanate ceramics
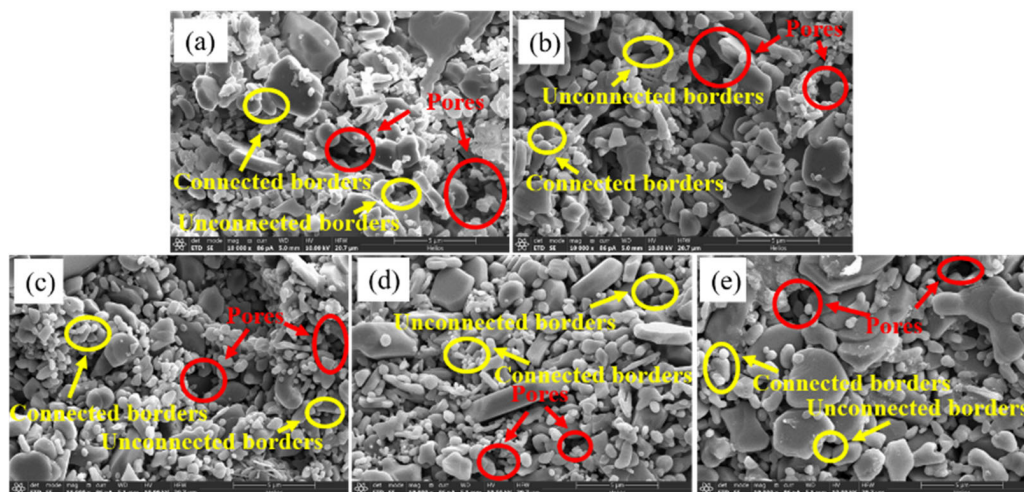
Fig. 4 SEM images of samples sintered at different temperatures: (a) 1150, (b) 1200, (c) 1250, (d) 1300, and (e) 1350 ℃.
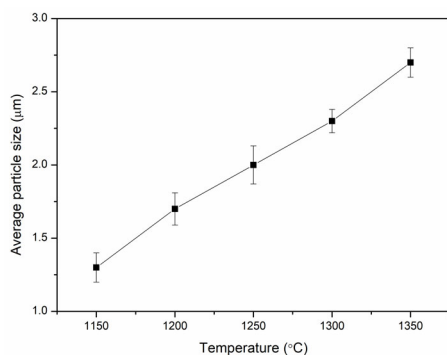

Fig. 5 Average particle size of alumina ceramic sintered at different temperatures.

and found that the average particle size increased significantly as the sintering temperature increased, whereas the average particle size was 0.7, 1.6, 3.0–8.0 μm when the sintering temperature was 800, 900, 1000 ℃, respectively. The increasing sintering temperature leading to increasing particle size can be explained using Eq. (2), showing the dependence of diffusion to sintering temperature [38]. The increased temperature leads to the increased diffusion coefficient, leading to the growth of particles.

$$D = D_0 \exp\left(\frac{-Q}{RT}\right) \tag{2}$$

where D is the diffusion coefficient, D_0 is a constant of diffusion, Q is the activation energy, R is Boltzmann's constant, and T is the test environment temperature.

By combining the flexural strength results described in the latter part, the sintering temperature should be at 1350 ℃. Then, the micromorphology of samples sintered at 1350 ℃ obtained from TEM is shown in Fig. 6. The

TEM images (Figs. 6(a) and 6(b)) show the presence of pores in the sintered samples, and some particles were connected together. The lattice fringe (Fig. 6(c)) of alumina ceramic is shown in the high-resolution transmission electron microscopy (HRTEM) image, and the lattice spacing is 0.155 nm, representing the (211) crystallographic plane of α-alumina. The selected-area electron diffraction pattern (Fig. 6(d)) indicates that the sintered alumina ceramics has a single crystal structure. The elemental distribution obtained from the TEM images of 1350 ℃ sintered samples is shown in Fig. 7. The elemental distribution images (Figs. 7(b) and 7(c)) show the uniform distribution of Al and O. The distribution of C (Fig. 7(d)) has the shape of copper microscope grid used to prepare the TEM samples. The EDS curve (Fig. 7(e)) indicates that the main elements in the samples are Al and O. Although the sintering process lacked oxygen, O was detected in the sample. This O might have arisen from the Al_2O_3; the debinding process would introduce some O atoms. The sample was composed of alumina, which containing O and Al. Though the sintering atmosphere was argon, there should be O in the sample after the sintering process. Therefore, the O element should be detected, and the oxygen peak could be seen in Fig. 7(e).

The XRD results of alumina ceramics sintered at different temperatures are shown in Fig. 8(a). The peaks of different samples are located at 25.6°, 35.1°, 37.8°, 41.7°, 43.4°, 46.2°, 52.6°, 57.5°, 59.8°, 61.2°, 66.5°, 68.2°, 70.4°, 74.3°, 77.2°, 80.7°, 84.4°, and 86.4°, belonging to (012), (104), (110), (006), (113), (202), (024), (116), (211), (122), (214), (300), (125),
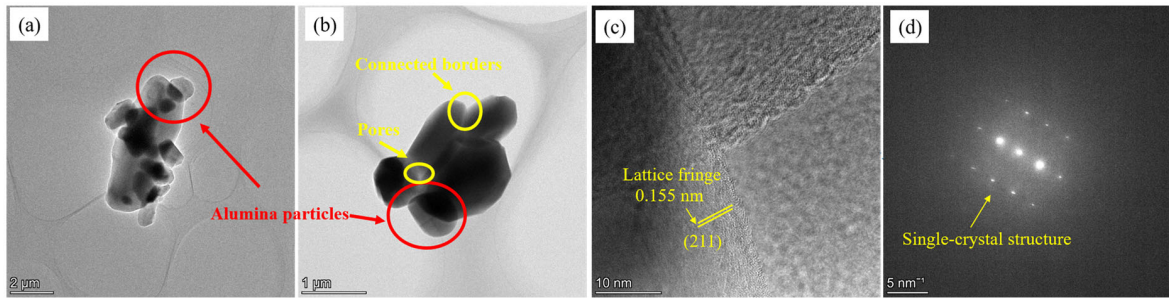
Fig. 6 TEM images of 1350 ℃ sintered samples: (a) TEM image, (b) TEM image, (c) HRTEM image, and (d) selected-area electron diffraction pattern.
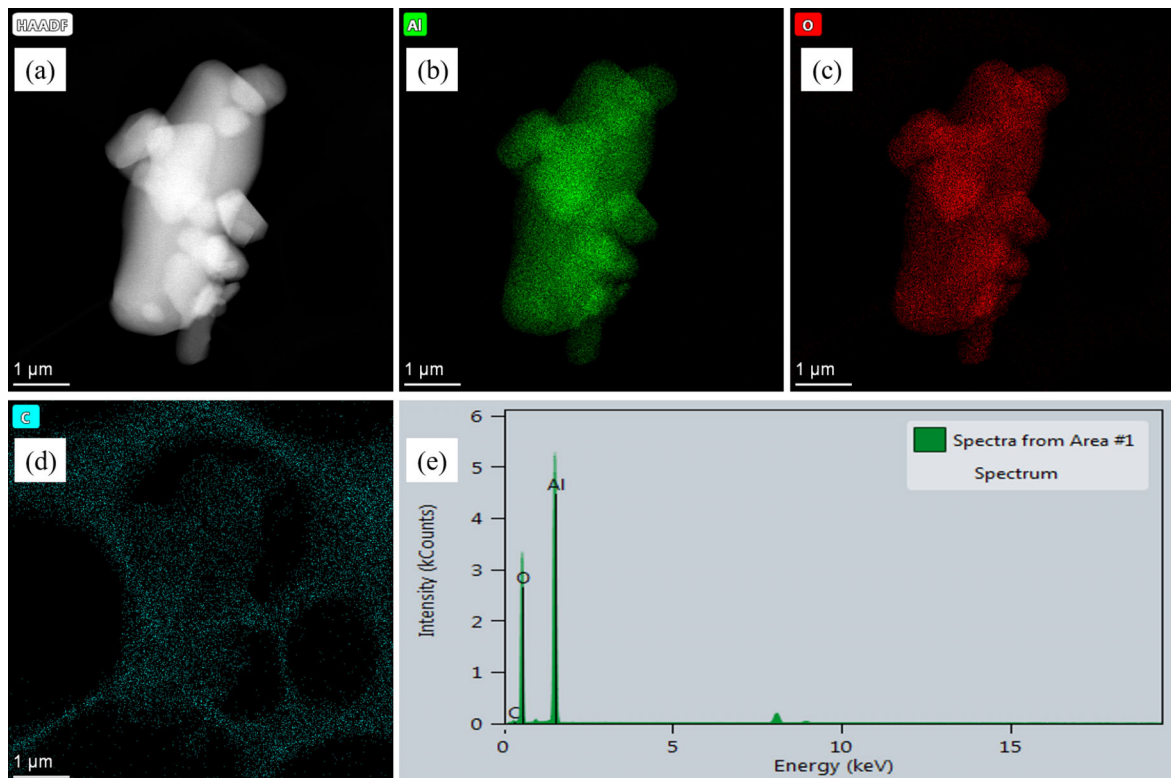

Fig. 7 Elemental distribution obtained from TEM images of 1350 ℃ sintered samples: (a) HAADF image, (b) distribution of Al element, (c) distribution of O element, (d) distribution of C element, and (e) EDS curve.
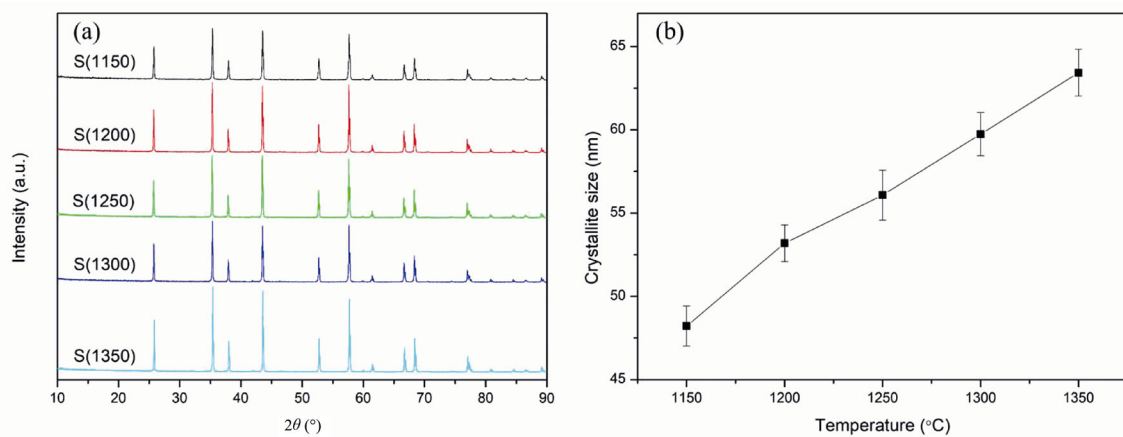

Fig. 8 XRD results of alumina ceramics sintered at different temperatures: (a) XRD curves and (b) crystallite size.

(208), (119), (220), (223), and (312) crystallographic planes (PDF#65-3103), respectively [39]. Figure 8(b) shows the trend of crystallite size of alumina ceramics with sintering temperature. The results indicate that the crystallite size increased from 48.2 to 63.4 nm with increasing sintering temperature from 1150 to 1350 ℃. A relatively higher sintering temperature would promote the growth of crystallite size for the sintered ceramic samples. This phenomenon was also observed in nonoxide ceramics, for example, Gubicza *et al.* [40] found that a higher sintering temperature promoted the growth of crystallite size for SiC ceramic, and the crystallite size was determined for sintering temperature.

According to the empirical formula shown in Eq. (3), the crystallite size would increase with the increase in temperature [41,42]. The sintering temperature was input into the formula, and the results are shown in Fig. 9. This indicates that the crystallite size would increase with increasing sintering temperature, consistent with the results shown in Fig. 8.

$$d^n - d_0^{\ n} = kt \exp\left(-\frac{Q}{RT}\right) \tag{3}$$

where d is the crystallite size after growth (nm), d_0 is the initial crystallite size (nm), k and t are physical constants related to specific materials, R is the universal gas constant, Q is the activation energy, and n is the constant for a given grain growth mechanism.

The Raman spectra of sintered samples are shown in Fig. 10. The peaks of samples sintered at different temperatures in argon are located at 378, 418, 432, 451, 578, 645, and 751 cm^{-1}, respectively, indicating that the samples belong to α-alumina [43–45].
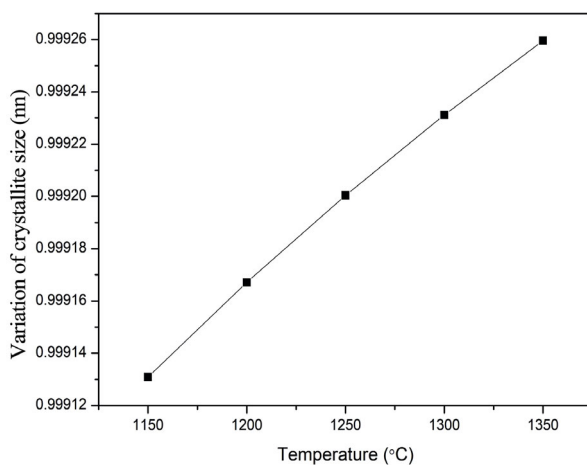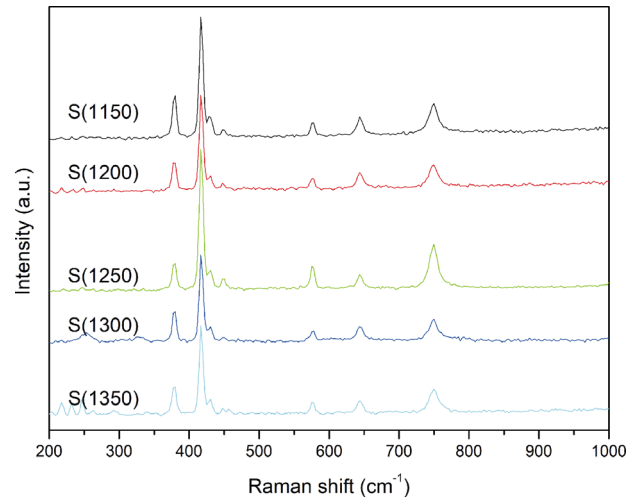

Fig. 10 Raman spectra of alumina ceramic sintered at different temperatures.

The XPS curves of alumina ceramic sintered at different temperatures in argon are shown in Fig. 11. The peaks located at 529, 117, and 72 eV represent the O 1s, Al 2s, and Al 2p, respectively. The results indicate that the sintering temperature slightly affects the state of chemical bonds. The atomic ratios obtained from the XPS of alumina ceramic sintered at different temperatures are shown in Table 1. This indicates that the elemental content of different samples is basically consistent, and the temperature does not affect the composition and content of each element. However, the ratio of O:Al was almost 1:1, indicating a lower O content for Al_2O_3. This is probably because of the lack of oxygen during the sintering temperature; the argon atmosphere might reduce the content of O atoms in the samples.
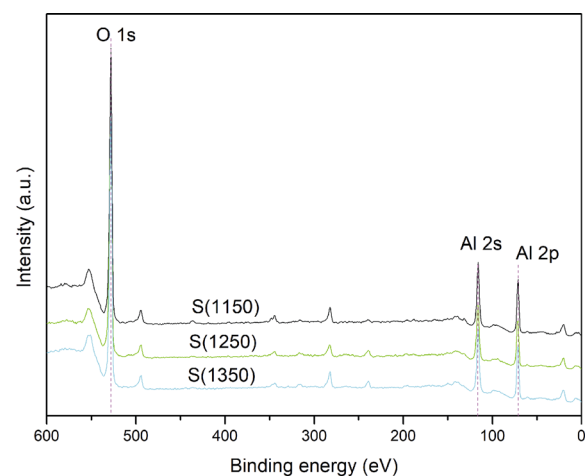

Fig. 9 Variation in crystallite size for alumina ceramics sintered at different temperatures.

Fig. 11 XPS curves of alumina ceramic sintered at different temperatures.

Table 1 Atomic ratio (XPS) of samples sintered at different temperatures

Sample ID	O	Al
S(1150)	54.02	45.98
S(1250)	52.80	47.20
S(1350)	52.98	47.02

3.2 Physical properties

The shrinkage of alumina ceramics sintered at different temperatures is shown in Fig. 12. The results show that the shrinkage increased with increasing sintering temperature. The shrinkage of *X* direction increased from 0.5% to 3.0% as the sintering temperature increased from 1150 to 1350 ℃; the shrinkage of *Y* direction increased from 0.7% to 3.2% as the sintering temperature increased from 1150 to 1350 ℃; the shrinkage of *Z* direction increased from 1.6% to 5.5% as the sintering temperature increased from 1150 to 1350 ℃. These results show that the shrinkage of *Z* direction is significantly greater than the shrinkage of *X* or *Y* directions, whereas the shrinkage of *Y* direction is slighter greater than the shrinkage of *X* direction. This was caused by the layer-by-layer forming characteristic derived from stereolithography-based 3D printing technology, a common phenomenon in sintered ceramics. The shrinkage phenomenon existed in most of the sintered ceramics. Gonzalez *et al.* [46] fabricated alumina ceramic with a shrinkage of 8.75% in the *X* direction, 10.92% in the *Y* direction, and 15.37% in the *Z* direction. He *et al.* [13] fabricated the zirconia ceramic parts with a shrinkage of 35.26% and believed that samples with different dimensions and shapes will display different shrinkage rates. Su *et al.* [47] fabricated alumina ceramic with sintering shrinkage of 12.0%, 15.1%, and 21.4% in the *X*, *Y*, and *Z* direction, respectively, and believed that the shrinkage in *Z* direction was the largest because of the "friction-free" state of green ceramic during sintering. There was no constraint to hinder the sintering shrinking in the *Z* direction. However, in the *X*–*Y* direction, the frictional constraint between the green bodies and porous setter may result in a mechanical interlocking effect and hinder the free shrinking and movement between the green bodies and setter materials in the sintering stage. This resulted in a much greater shrinkage in the *Z* direction than *X* or *Y* directions [48].
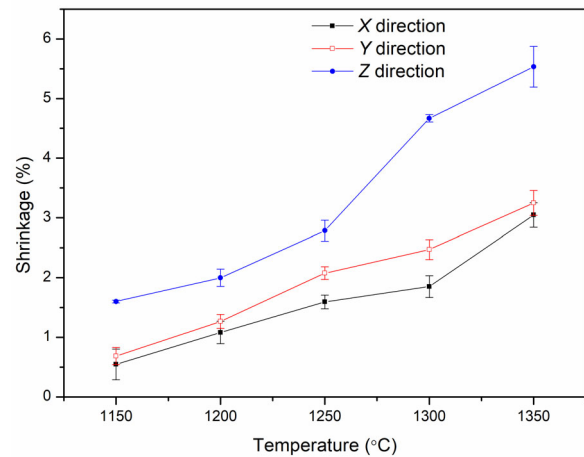

Fig. 12 Shrinkage of alumina ceramic sintered at different temperatures.

The bulk density and open porosity of samples sintered at different temperatures are shown in Fig. 13. Bulk density increased with increasing sintering temperature, whereas open porosity decreased with increasing sintering temperature. The bulk density increased from 2.3 to 2.5 g/cm^3 and the open porosity decreased from 39.0% to 33.8% as the sintering temperature increased from 1150 to 1350 ℃. This phenomenon indicates that sintering temperature significantly affects the bulk density and open porosity of alumina ceramics. During sintering, a higher sintering temperature could promote the densification of alumina ceramics along with the migration of particles, rearrangement, and shrinkage, leading to the variation of bulk density and open porosity. According to Wang *et al.* [49], the bulk density of alumina–zirconia ceramics rapidly increases as the sintering temperature increases because of its high densification rate; they concluded that surface diffusion is recognized to be unfavorable for the densification process. Khattab *et al.* [50] found that the bulk density of alumina ceramics is dependent on sintering temperature, and the increase in temperature enhanced the sintering of samples as well as each alumina grains near from others, resulting a decrease in the distance between alumina grains and alumina grain growth. Then, the open porosity decreased. Ding *et al.* [51] prepared porous mullite ($3Al_2O_3 \cdot 2SiO_2$) ceramics and found that the open porosity decreases and the bulk density increases with increasing sintering temperature because of the enhancement of viscous flow of SiO_2. However, some ceramics exhibited opposite phenomenon. Dong *et al.* [52] prepared mineral-based mullite ceramics and found that the bulk density decreases with increasing sintering temperature because
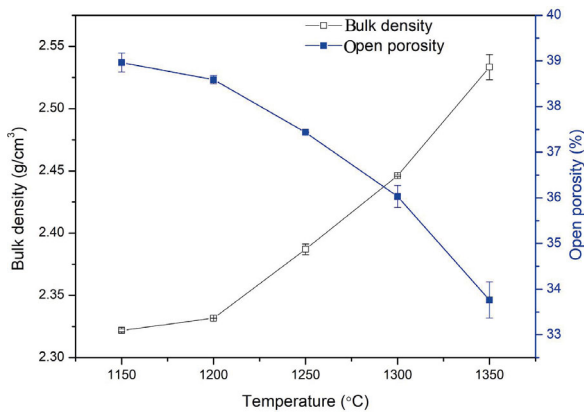
Fig. 13 Bulk density and open porosity of samples sintered at different temperatures.

unique self-expansion occurred between 1326 and 1477 ℃. Open porosity increases with increasing sintering temperature, indicating an important effect on sintering self-expansion on microstructure.

3. 3 Mechanical properties

The mechanical properties of samples sintered at different temperatures are shown in Fig. 14, including flexural strength, Vickers hardness, load–displacement curves, and nanoindentation hardness. Figure 14(a) shows that the flexural strength increased from 5.8 to 26.7 MPa as the sintering temperature increased from 1200 to 1350 ℃. Figures 14(b)–14(d) show that the Vickers hardness increased from 107.9 to 198.5 HV, and the hardness obtained from nanoindentation test increased from 13.4 to 33.1 GPa as the sintering temperature increased from 1150 to 1350 ℃. These results indicate that the flexural strength and hardness of alumina ceramics increase with increasing sintering temperature in the range of 1150–1350 ℃. According to Zhu *et al*. [53], the flexural strength of porous alumina increased with increasing sintering temperature. The flexural strength of porous ceramics depends on the sintering neck areas among the grains and the amount of sintering necks [54–56]. Along with the increase in sintering temperature, the growth of sintering necks and sintering densification are promoted, increasing the flexural strength and decreasing the porosity.
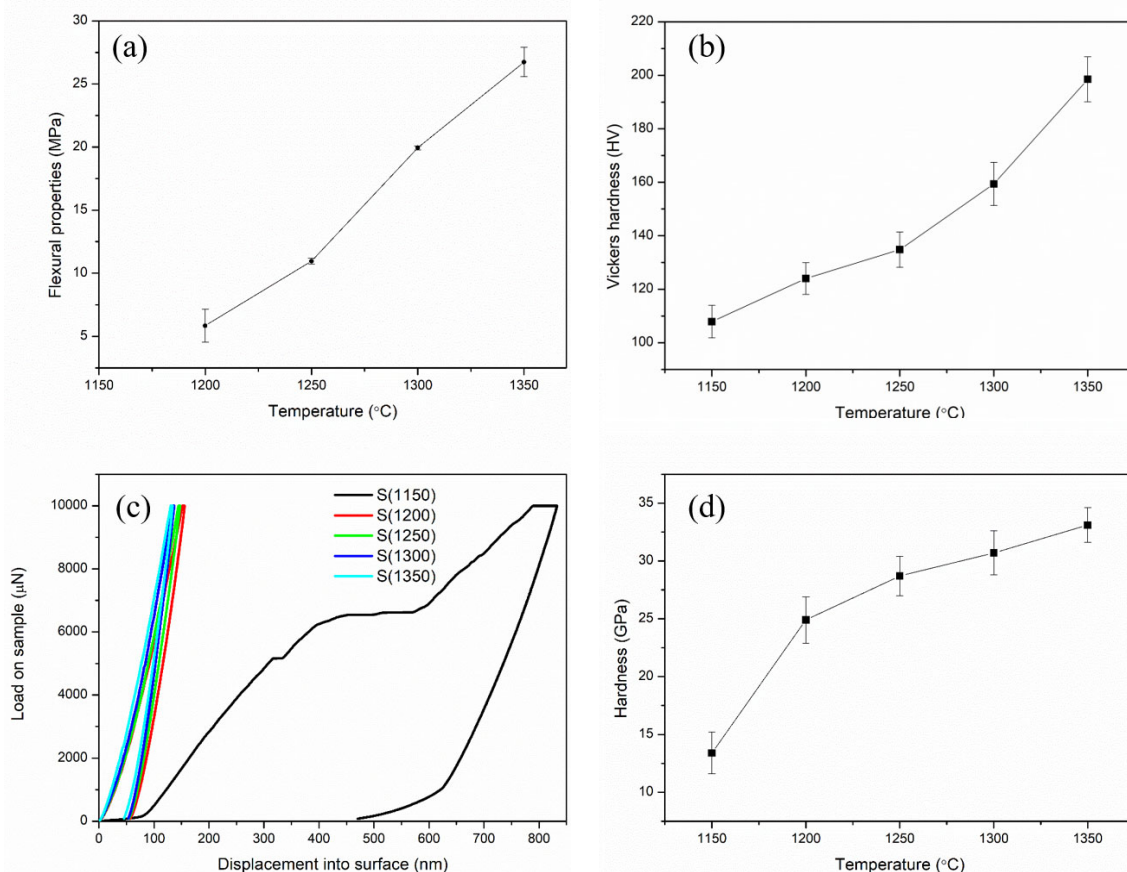

Fig. 14 Mechanical properties of samples sintered at different sintering temperatures: (a) flexural strength, (b) Vickers hardness, (c) load–displacement curves from nanoindentation tests, and (d) hardness obtained from nanoindentation tests.
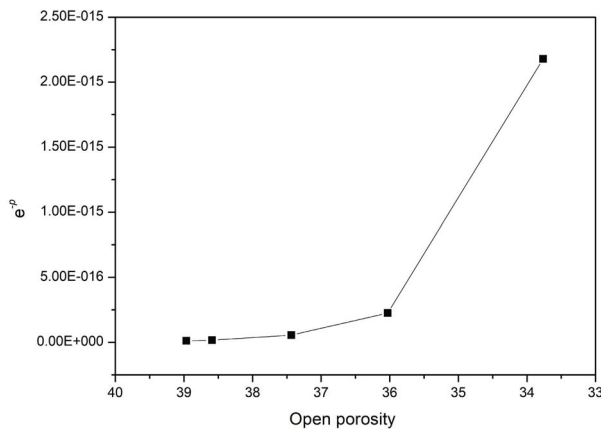
Fig. 15 Variation of strength with open porosity.

According to Ryskewitsch equation [57] shown as follows, the flexural strength of ceramic decreases with the increase in porosity.

$$\sigma = \sigma_0 \exp(-\alpha p) \qquad (4)$$

where σ is the strength (MPa), $\sigma \propto \exp(-p)$, σ_0 is the strength of porosity at 0 (MPa), p is the porosity (%), and α is a constant of the flexural strength. By substituting the value of porosity derived from Fig. 13 into Eq. (4), the results are shown in Fig. 15. The flexural strength increased as the open porosity decreased, whereas the open porosity decreased with increasing sintering temperature. Then, the flexural strength increased with the increasing of sintering temperature, consistent with the results shown in Fig. 14(a). The hardness of alumina ceramic mainly depends on the crystal structure and microstructure of alumina ceramics. The variation tendency of hardness is similar to the flexural strength, mainly depending on the sintering temperature.

4   Conclusions

The effect of sintering temperature in argon atmosphere on the microstructure, and physical and mechanical properties of 3D printed alumina ceramics was evaluated, aiming to apply alumina ceramic in the fabrication of alumina ceramic core. The results show that the average particle size, shrinkage, bulk density, crystallite size, flexural strength, Vickers hardness, and nanoindentation hardness increased with the increasing sintering temperature. The open porosity decreased with the increasing sintering temperature. Sintering temperature slightly affects the phase composition, chemical bonding,

and atomic ratio. The samples are made of layers, and the shrinkage of Z direction is much greater than those of X or Y directions due to the layer-by-layer forming method. 1350 ℃ is considered as the optimum sintering temperature in argon atmosphere with a shrinkage of 3.0% in X direction, 3.2% in Y direction, and 5.5% in Z direction, flexural strength of 26.7 MPa, Vickers hardness of 198.5 HV, nanoindentation hardness of 33.1 GPa, bulk density of 2.5 g/cm^3, and open porosity of 33.8%. The 3D printed alumina ceramics sintered at 1350 ℃ in argon atmosphere satisfy the requirement of alumina ceramic cores.

Acknowledgements

References

[1]   Gromada M, Świeca A, Kostecki M, *et al*. Ceramic cores for turbine blades via injection moulding. *J Mater Process Technol* 2015, **220**: 107–112.

[2]   Chen ZW, Li ZY, Li JJ, *et al*. 3D printing of ceramics: A review. *J Eur Ceram Soc* 2019, **39**: 661–687.

[3]   Wu HH, Li DC, Tang YP, *et al*. Gelcasting of alumina based ceramic cores containing yttria for single crystal and directional solidification blades. *Adv Appl Ceram* 2009, **108**: 406–411.

[4]   Kato T, Ushijima H, Katsumata M, *et al*. Effect of core materials on the formation of hollow alumina microspheres by mechanofusion process. *J Am Ceram Soc* 2004, **87**: 60–67.

[5]   Kazemi A, Faghihi-Sani MA, Alizadeh HR. Investigation on cristobalite crystallization in silica-based ceramic cores for investment casting. *J Eur Ceram Soc* 2013, **33**: 3397–3402.

[6]   Ferrage L, Bertrand G, Lenormand P, *et al*. A review of the additive manufacturing (3DP) of bioceramics: Alumina, zirconia (PSZ) and hydroxyapatite. *J Aust Ceram Soc* 2017, **53**: 11–20.

[7]   Cheng ZL, Ye F, Liu YS, *et al*. Mechanical and dielectric properties of porous and wave-transparent Si$_3$N$_4$-Si$_3$N$_4$ composite ceramics fabricated by 3D printing combined with chemical vapor infiltration. *J Adv Ceram* 2019, **8**: 399–407.

[8]   Tangcharoen T, T-Thienprasert J, Kongmark C. Effect of calcination temperature on structural and optical properties of MAl$_2$O$_4$ (M = Ni, Cu, Zn) aluminate spinel nanoparticles. *J Adv Ceram* 2019, **8**: 352–366.

[9]   Liu JJ, Huo WL, Zhang XY, *et al*. Optimal design on the

high-temperature mechanical properties of porous alumina ceramics based on fractal dimension analysis. *J Adv Ceram* 2018, **7**: 89–98.

[10] Liu K, Zhang K, Bourell DL, *et al*. Gelcasting of zirconia-based all-ceramic teeth combined with stereolithography. *Ceram Int* 2018, **44**: 21556–21563.

[11] Chen ZW, Liu CB, Li JJ, *et al*. Mechanical properties and microstructures of 3D printed bulk cordierite parts. *Ceram Int* 2019, **45**: 19257–19267.

[12] Liu K, Zhang K, Bourell DL, *et al*. Gelcasting of zirconia-based all-ceramic teeth combined with stereolithography. *Ceram Int* 2018, **44**: 21556–21563.

[13] He RX, Liu W, Wu ZW, *et al*. Fabrication of complex-shaped zirconia ceramic parts via a DLP-stereolithography-based 3D printing method. *Ceram Int* 2018, **44**: 3412–3416.

[14] Lu ZL, Tian GQ, Wan WJ, *et al*. Effect of *in situ* synthesised mullite whiskers on the high-temperature strength of Al_2O_3-based ceramic moulds for casting hollow turbine blades. *Ceram Int* 2016, **42**: 18851–18858.

[15] Wu P, Xu YZ, Huang ZX, *et al*. A review of preparation techniques of porous ceramic membranes. *J Ceram Process Res* 2015, **16**: 102–106.

[16] An GS, Choi SW, Kim TG, *et al*. Amino-functionalization of colloidal alumina particles for enhancement of the infiltration behavior in a silica-based ceramic core. *Ceram Int* 2017, **43**: 157–161.

[17] Xu FF, Ren H, Zheng MJ, *et al*. Development of biodegradable bioactive glass ceramics by DLP printed containing EPCs/BMSCs for bone tissue engineering of rabbit mandible defects. *J Mech Behav Biomed Mater* 2020, **103**: 103532.

[18] Li H, Liu YS, Liu YS, *et al*. Thermal treatment of γ-Al_2O_3 for the preparation of stereolithography 3D printing ceramic slurries. *Front Mater* 2019, **6**: 295.

[19] Li H, Liu YS, Liu YS, *et al*. Evolution of the microstructure and mechanical properties of stereolithography formed alumina cores sintered in vacuum. *J Eur Ceram Soc* 2019. DOI 10.1016/j.jeurceramsoc.2019.11.047.

[20] Evernden JF, Curtis GH, Kistler RW, *et al*. Argon diffusion in glauconite, microcline, sanidine, leucite and phlogopite. *Am J Sci* 1960, **258**: 583–604.

[21] Barrosse-Antle LE, Aldous L, Hardacre C, *et al*. Dissolved argon changes the rate of diffusion in room temperature ionic liquids: Effect of the presence and absence of argon and nitrogen on the voltammetry of ferrocene. *J Phys Chem C* 2009, **113**: 7750–7754.

[22] Li H, Liu YS, Liu YS, *et al*. Influence of sintering temperature on microstructure and mechanical properties of Al_2O_3 ceramic via 3D stereolithography. *Acta Metall Sin (Engl Lett)* 2020, **33**: 204–214.

[23] Ben Ayed F, Bouaziz J, Bouzouita K. Calcination and sintering of fluorapatite under argon atmosphere. *J Alloys Compd* 2001, **322**: 238–245.

[24] Mandal S, Sanyal AS, Dhargupta KK, *et al*. Gas pressure sintering of β SiC–γ-AlON composite in nitrogen/argon

environment. *Ceram Int* 2001, **27**: 473–479.

[25] Mulla MA, Krstic VD. Pressureless sintering of β-SiC with Al_2O_3 additions. *J Mater Sci* 1994, **29**: 934–938.

[26] Moon JH, Jang HM. Effects of sintering atmosphere on densification behavior and piezoelectric properties of $Pb(Ni_{1/3}Nb_{2/3})O_3$-$PbZrO_3$ ceramics. *J Am Ceram Soc* 1993, **76**: 549–552.

[27] He H, Lou J, Li YM, *et al*. Effects of oxygen contents on sintering mechanism and sintering-neck growth behaviour of FeCr powder. *Powder Technol* 2018, **329**: 12–18.

[28] Dargatz B, Gonzalez-Julian J, Bram M, *et al*. FAST/SPS sintering of nanocrystalline zinc oxide—Part II: Abnormal grain growth, texture and grain anisotropy. *J Eur Ceram Soc* 2016, **36**: 1221–1232.

[29] Mazloumi M, Khalifehzadeh R, Sadrnezhaad SK, *et al*. Alumina nanopowder production from synthetic bayer liquor. *J Am Ceram Soc* 2006, **89**: 3654–3657.

[30] Sun J, Gao L, Jin XH. Reinforcement of alumina matrix with multi-walled carbon nanotubes. *Ceram Int* 2005, **31**: 893–896.

[31] Seabaugh MM, Kerscht IH, Messing GL. Texture development by templated grain growth in liquid-phase-sintered α-alumina. *J Am Ceram Soc* 2005, **80**: 1181–1188.

[32] Osorio E, Toledano M, da Silveira BL, *et al*. Effect of different surface treatments on In-Ceram Alumina roughness. An AFM study. *J Dent* 2010, **38**: 118–122.

[33] Lofaj F, Ferdinandy M, Cempura G, *et al*. Nanoindentation, AFM and tribological properties of thin nc-WC/a-C Coatings. *J Eur Ceram Soc* 2012, **32**: 2043–2051.

[34] Schwentenwein M, Homa J. Additive manufacturing of dense alumina ceramics. *Int J Appl Ceram Technol* 2015, **12**: 1–7.

[35] Bertsch A, Jiguet S, Renaud P. Microfabrication of ceramic components by microstereolithography. *J Micromech Microeng* 2004, **14**: 197–203.

[36] Hahn H, Logas J, Averback RS. Sintering characteristics of nanocrystalline TiO_2. *J Mater Res* 1990, **5**: 609–614.

[37] Pookmanee P, Rujijanagul G, Ananta S, *et al*. Effect of sintering temperature on microstructure of hydrothermally prepared bismuth sodium titanate ceramics. *J Eur Ceram Soc* 2004, **24**: 517–520.

[38] Conrad H. Effects of electric current on solid state phase transformations in metals. *Mat Sci Eng-A* 2000, **287**: 227–237.

[39] Eklund P, Sridharan M, Sillassen M, *et al*. α-Cr_2O_3 template-texture effect on α-Al_2O_3 thin-film growth. *Thin Solid Films* 2008, **516**: 7447–7450.

[40] Gubicza J, Nauyoks S, Balogh L, *et al*. Influence of sintering temperature and pressure on crystallite size and lattice defect structure in nanocrystalline SiC. *J Mater Res* 2007, **22**: 1314–1321.

[41] Onn TM, Zhang SY, Arroyo-Ramirez L, *et al*. High-surface-area ceria prepared by ALD on Al_2O_3 support. *Appl Catal B: Environ* 2017, **201**: 430–437.

[42] Tekeli S. Fracture toughness (K_{IC}), hardness, sintering and

grain growth behaviour of 8YSCZ/Al$_2$O$_3$ composites produced by colloidal processing. *J Alloys Compd* 2005, **391**: 217–224.

[43] Kadleíková M, Breza J, Veselý M. Raman spectra of synthetic sapphire. *Microelectron J* 2001, **32**: 955–958.

[44] Reyes-López SY, Acuña RS, López-Juárez R, *et al*. Analysis of the phase transformation of aluminum formate Al(O$_2$CH)$_3$ to α-alumina by Raman and infrared spectroscopy. *J Ceram Proc Res* 2013, **14**: 627–631.

[45] Mariotto G, Cazzanelli E, Carturan G, *et al*. Raman and X-ray diffraction study of boehmite gels and their transformation to α- or β-alumina. *J Solid State Chem* 1990, **86**: 263–274.

[46] Gonzalez JA, Mireles J, Lin Y, *et al*. Characterization of ceramic components fabricated using binder jetting additive manufacturing technology. *Ceram Int* 2016, **42**: 10559–10564.

[47] Su B, Dhara S, Wang L. Green ceramic machining: A top-down approach for the rapid fabrication of complex-shaped ceramics. *J Eur Ceram Soc* 2008, **28**: 2109–2115.

[48] Ighodaro OL, Okoli OI, Zhang M, *et al*. Ceramic preforms with 2D regular channels for fabrication of metal/ceramic-reinforced composites. *Int J Appl Ceram Tec* 2012, **9**: 421–430.

[49] Wang CJ, Huang CY, Wu YC. Two-step sintering of fine alumina–zirconia ceramics. *Ceram Int* 2009, **35**: 1467–1472.

[50] Khattab RM, Wahsh MMS, Khalil NM. Preparation and characterization of porous alumina ceramics through starch consolidation casting technique. *Ceram Int* 2012, **38**: 4723–4728.

[51] Ding SQ, Zeng YP, Jiang DL. Fabrication of mullite ceramics with ultrahigh porosity by gel freeze drying. *J Am Ceram Soc* 2007, **90**: 2276–2279.

[52] Dong YC, Zhou JE, Lin B, *et al*. Reaction-sintered porous mineral-based mullite ceramic membrane supports made from recycled materials. *J Hazard Mater* 2009, **172**: 180–186.

[53] Zhu ZW, Xiao J, He W, *et al*. A phase-inversion casting process for preparation of tubular porous alumina ceramic membranes. *J Eur Ceram Soc* 2015, **35**: 3187–3194.

[54] Chang QB, Yang YL, Zhang XZ, *et al*. Effect of particle size distribution of raw powders on pore size distribution and bending strength of Al$_2$O$_3$ microfiltration membrane supports. *J Eur Ceram Soc* 2014, **34**: 3819–3825.

[55] Mieller B. Influence of test procedure on dielectric breakdown strength of alumina. *J Adv Ceram* 2019, **8**: 247–255.

[56] Zou J, Zhong Y, Zhang JZ, *et al*. Separating macrostresses from microstresses in Al$_2$O$_3$–15vol%SiC particulate reinforced composites. *Scr Mater* 2015, **109**: 84–88.

[57] Glasser FP. Advances in the performance of cement-based systems. In *Advanced Ceramics III*. Sōmiya S, Ed. Elsevier Science Publishers, 1990: 157–161.